

# Surface image and activity-corrected orbit of the RS CVn binary HR 7275

## Disentangling activity tracers

Ö. Adebali<sup>1,2</sup>\*, M. Weber<sup>1</sup>, K. G. Strassmeier<sup>1,2</sup>, I. V. Ilyin<sup>1</sup>, M. Steffen<sup>1</sup>, and Zs. Kővári<sup>3,4</sup>

<sup>1</sup> Leibniz-Institute for Astrophysics Potsdam (AIP), An der Sternwarte 16, D-14482 Potsdam, Germany

<sup>2</sup> Institut für Physik und Astronomie, Universität Potsdam, D-14476 Potsdam, Germany

<sup>3</sup> HUN-REN Research Centre for Astronomy and Earth Sciences, Konkoly Observatory, H-1121 Budapest, Hungary

<sup>4</sup> HUN-REN CSFK, MTA Centre of Excellence, H-1121 Budapest, Hungary

Received: 16 October 2025 / Accepted: 10 December 2025

## ABSTRACT

**Context.** Quantifying stellar parameters and magnetic activity for cool stars in double-lined spectroscopic binaries (SB2) is not straightforward, as both stars contribute to the observed composite spectra and are likely variable. Disentangled component spectra allow a detailed analysis of a component's magnetic activity.

**Aims.** We aim at separating the spectra of the two stellar components of the HR 7275 SB2 system. Our further aim is a more accurate orbital solution by cleaning the observed radial velocities (RV) from activity perturbations of the spotted primary ("RV jitter") and obtain a surface image of this component.

**Methods.** We provide time-series high- and ultra-high resolution optical spectra and apply two different disentangling methods. RV residuals are modeled with three-sine function fits. The primary's spectral-line profiles are modeled with the Doppler imaging code *iMAP*. Magnetic fields are measured for the primary based on least-square deconvolved Stokes-V line profiles. Chromospheric emission is determined from the line-cores of Ca II H&K, Ca II IRT 8542 Å, and Balmer H $\alpha$ . Before applying those analyses, we provide a disentangling technique to determine the system properties more accurately.

**Results.** The Doppler image of the primary shows two large cool spots of size  $\approx 20\%$  of the visible hemisphere plus three smaller spots, each still  $\approx 13\%$  in size. In total, HR 7275a exhibited an impressive spottedness of  $\approx 40\%$  of its entire surface in May-June 2022. The RV is modulated by the rotation of the primary with maximum amplitudes of  $320 \text{ m s}^{-1}$  and  $650 \text{ m s}^{-1}$  for two different modulation behaviors during the 250 d of our observations. This jitter is primarily caused by the varying asymmetries of the apparent disk brightness due to the cool spots. Its removal resulted in roughly ten times higher precision of the orbital elements. Our snapshot magnetic-field measurements reveal phase-dependent (large-scale) surface fields between  $+0.6 \pm 2.0 \text{ G}$  at phase 0.1 and  $-15.2 \pm 2.7 \text{ G}$  at phase 0.6, indicating a complex magnetic morphology related to the location of the photospheric spots. We also obtain a logarithmic lithium abundance of  $0.58 \pm 0.1$  for HR 7275a, indicating considerable mixing, and  $0.16_{-0.63}^{+0.23}$  for HR 7275b, which is an extremely low value.

**Key words.** stars: binaries: spectroscopic – stars: activity – stars: RS CVn – techniques: radial velocity – techniques: activity correction – techniques: Doppler imaging – techniques: spectroscopy – techniques: spectropolarimetry – techniques: chemical abundances – techniques: spectral disentangling

## 1. Introduction

Starspots are important indicators of stellar activity, providing information about the underlying magnetic dynamo in late-type stars. These features allow us to track the operation of magnetic activity, as well as activity processes associated with different atmospheric layers (such as the photosphere and chromosphere).

Active components with huge starspots in RS CVn type binary systems offer an excellent opportunity to monitor such activity processes. These systems were first described and studied in depth by Hall (1972), and then Vogt & Penrod (1983) applied the groundbreaking Doppler imaging technique to cool stars, opening up entirely new horizons. The first detailed catalog of active binary stars was compiled by Strassmeier et al. (1993). The study of these RS CVn stars has yielded several fundamental results regarding the relationship between photospheric starspots

and global magnetic activity (e.g., Strassmeier 2009). Continuing the series, in our paper we take a closer look at the activity of another RS CVn system, HR 7275, and attempt to separate the activity signals from the precise orbital solution.

HR 7275 is a binary system with a tidally locked primary with an orbital and rotational period of  $\approx 28$  d, which has been confirmed by various authors using photometric methods (Fried et al. 1982; Strassmeier et al. 1989) and RV measurements (Young 1944; Eker 1989; Osten & Saar 1998; de Medeiros & Udry 1999). It is a bright-star-catalog target with visual magnitude of 5.89 (Ducati 2002) that makes it easy to observe. The system is an SB2 with a K2IV-III type (sub)giant primary accompanied by a warm G type secondary. The mass of the primary was determined by Eker (1989) to be between  $1-3 M_{\odot}$  and the stellar radius was given by Osten & Saar (1998) as  $6.2 R_{\odot}$  with a surface temperature of 4500 K. The rotational line broadening ( $v \sin i$ ) was measured to about  $15 \text{ km s}^{-1}$  (e.g., Osten & Saar

\* Corresponding author; oadebali@aip.de

1998; de Medeiros & Udry 1999). Initially considering the system as a single-lined binary (SB1), orbital solutions were given by Young (1944) and Eker (1989). An SB2 solution was first reported by Osten & Saar (1998) and then revised shortly afterwards by de Medeiros & Udry (1999). Based on the solutions by Eker (1989), the secondary star has a mass of  $0.9\text{--}1.1 M_{\odot}$  and a surface temperature of 5500 K is found by Osten & Saar (1998).

In the case of an SB2 system like HR 7275, spectral disentangling is the first step before determining precise stellar parameters. There are several different technical approaches for this purpose (e.g. Hensberge et al. 2008; Weber & Strassmeier 2011; Sablowski et al. 2019). Osten & Saar (1998) used a grid of template stars to fit the components of the HR 7275 system in the combined spectrum. A similar technique, but with a synthetic spectral grid, was used by Weber & Strassmeier (2011) for Capella ( $\alpha$  Aur), a system of two G giants. An iterative technique, called the direct spectral decomposition, was developed by Folsom et al. (2010) and successfully applied to the eclipsing binary AR Aur. Another iterative method, the experiment of Kriskovics et al. (2013), in which a spectral disentangling technique was combined with Doppler imaging in order to recover the surface temperature maps for both components of the SB2 pre-main-sequence system V824 Ara should be mentioned.

TiO lines are often used to give estimates of starspot coverage and temperatures (Neff et al. 1995). Using this method, O’Neal et al. (1996) studied five active and evolved stars, including HR 7275, for which they determined a spot temperature of 3600 K with a filling factor of 31%. However, starspots, in addition to being tracers of activity-related magnetic phenomena, can also degrade the accuracy of spectroscopic RV measurements. Moreover, in a recent work by Strassmeier et al. (2024), it was shown that spots not only interfere with RV measurements, but also in the case of not very distant objects, such as the spotted giant XX Tri, significant rotation-induced stellar photocenter variations appear, which impose limitations, e.g., for astrometric-based exoplanet searches. Thus, for precise orbital calculations, these effects must be taken into account, especially when detecting a third companion, such as an exoplanet or a third body in a binary system. Saar & Donahue (1997) showed that starspots can produce RV perturbations of up to  $200 \text{ m s}^{-1}$ , while Hatzes (2002) demonstrated that these perturbations correlate with  $v \sin i$  (up to  $13 \text{ km s}^{-1}$  in their simulations) and the spot-filling factor. Desort et al. (2007) also showed how a single spot on a Sun-like star affects the line bisector variations. While their simulations allowed only a single spot, Boisse et al. (2011) used a more sophisticated two-spot model with which they also performed inclination tests. Most recently, Zhao & Dumusque (2023) have come up with a code called SOAP-GPU that allows the user to efficiently model stellar activity at the spectral level, even for complex activity region configurations. Finally, based on ultra-high resolution spectroscopic data of the RS CVn system  $\lambda$  And, we demonstrated the effect of starspots on RV measurements based on real observations, which we then took into account when correcting the orbital elements of the binary (Adebal et al. 2025).

The structure of this paper is as follows. In Sect. 2 we present our observations and the data reduction process. In Sect. 3 our spectral disentangling routines are described in detail, along with the RV calculations and the starspot correction required to make the orbital solution more accurate. The process of Doppler imaging is presented in Sect. 4, while the investigation of chromospheric activity is covered in Sect. 5, together with obtained magnetic field measurements and lithium abundance analyses. We summarize and conclude on our findings in Sect. 6.

## 2. Observations and data reduction

### 2.1. SES@STELLA

By using the 1.2-m STELLA (STELLar Activity) robotic telescope (Strassmeier et al. 2004) with the STELLA Echelle Spectrograph (SES), we obtained in total 148 high-resolution ( $R=55,000$ ) and high signal-to-noise ratio (S/N) spectra. Data with STELLA were autonomously collected once per clear night during the observing seasons 2021 and 2022. The SES is a fixed-format echelle spectrograph equipped with an e2v  $4\text{k}\times 4\text{k}$  CCD featuring  $15 \mu\text{m}$  pixels and a fiber-fed structure. The spectral resolution with a sampling of three pixels per resolution element is achieved through a 2-slice image slicer and a  $67 \mu\text{m}$  octagonal fiber that projects to 3.8 arc seconds on the sky. The wavelength coverage is from 3900 to 8800 Å. This corresponds to an effective resolution of  $110 \text{ m}\text{\AA}$ , or  $5.5 \text{ km s}^{-1}$  at  $6000 \text{ \AA}$ . Typical observations used an integration time of 280 s, yielding an average S/N of about 400 per pixel. Although the spectrograph is housed thermally, it is not pressure stabilized, resulting in a radial-velocity stability of at best  $30 \text{ m s}^{-1}$  (Strassmeier et al. 2023).

The SES data reduction pipeline is based on IRAF and described in detail in Weber et al. (2016). The CCD images were corrected for bad pixels and cosmic-ray impacts. Bias levels were removed by subtracting the average overscan from each image followed by the subtraction of the mean of the (already overscan subtracted) master bias frame. The target spectra were flattened by dividing by a nightly master flat. After removal of the scattered light, the one-dimensional spectra were extracted using the standard IRAF optimal extraction routine. The blaze function was then removed from the target spectra, followed by a wavelength calibration using consecutively recorded Th-Ar spectra. Finally, the extracted spectral orders were continuum normalized by dividing with a flux-normalized synthetic spectrum.

### 2.2. PEPSI@VATT and PEPSI-POL@LBT

The 1.8-m Vatican Advanced Technology Telescope (VATT) was used in combination with the Large Binocular Telescope’s (LBT) Potsdam Echelle Polarimetric and Spectroscopic Instrument (PEPSI; Strassmeier et al. 2015). PEPSI is a stabilized and fiber-fed echelle spectrograph having two arms (red and blue) with three cross dispersers (CD) for each arm. For HR7275, we employed only three of the six CDs (CD III+CD V and CD III+CD VI). Their wavelength regions covered were 4800–5440 Å (CD III) and 6278–9067 Å (CD V&VI). In its VATT mode the spectrograph provides a two-pixel resolution of  $R=250,000$ . The instrument resides in the basement of the LBT with a fiber connection of 450 m from the VATT. The VATT had been operated manually each night between UT May 10, 2022 and June 14, 2022, and thus covered one full rotation of the target star sampled by 28 spectra.

High-resolution Stokes IQUV spectra of HR 7275 were obtained on three separate nights, July 7, October 15, and October 22, 2024, using the PEPSI polarimeter with the 11.8-m LBT (PEPSI-POL). Circular polarization measurements were carried out with a super-achromatic quarter-wave retarder paired with a Foster prism serving as the polarizing beam-splitter. Observations were taken at two retarder positions, offset by  $90^\circ$ , and processed using the differential method outlined by Ilyin (2012), producing the Stokes I and V spectra discussed in Sect. 5. These polarimetric observations achieved a resolving power of 130,000 (2-pixel sampling), with a combined S/N of up to 3700:1 per

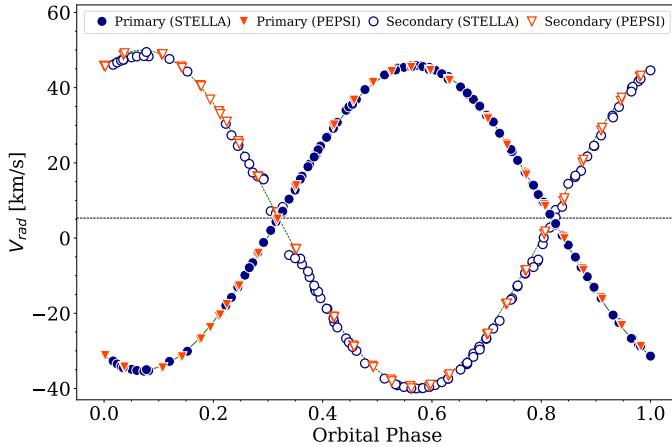


**Fig. 1.** Phase folded radial velocities for both stars in the system. Circle data points indicate the STELLA observations; triangle data points show PEPSI observations. The green lines (solid and dashed) represent the orbital fit while the black dashed line is the center of mass velocity.

pixel in the red wavelengths of the Stokes-I spectra, based on six sub-exposures per dataset.

VATT and LBT PEPSI data were reduced using the SDS4PEPSI package (“Spectroscopic Data Systems for PEPSI”), which is based on [Ilyin \(2000\)](#) and further detailed in [Strassmeier et al. \(2018, 2015\)](#). The reduction procedure comprises several image-processing steps: starting with bias subtraction and variance estimation of the raw frames, followed by super-master flat fielding to correct CCD spatial noise and the subtraction of scattered light. The pipeline then identifies the echelle orders and computes the wavelength solution from ThAr calibration images. Afterward, the optimal extraction of the image slicers is performed, along with the removal of cosmic spikes. The extracted spectra are normalized using the master flat-field spectrum to eliminate both CCD fringes and the blaze function. Finally, a global 2D continuum fit is applied, and all orders are rectified into a one-dimensional spectrum.

### 3. Data analysis

The observed spectra are analyzed using different techniques. First, we disentangle the two components to get a clearer picture of the activity behavior of the primary star. Then, we apply two different orbital solutions, both before and after the activity correction on the RV data points. The details of those processes are as follows.

#### 3.1. Spectral disentangling with DISTRACT

Because HR 7275 is an SB2 system, we search for the orbit of the secondary component by disentangling the spectra, using the code we developed for this purpose. DISTRACT (DIsentangler for STELLA ACTivity) consists of two different techniques for the two datasets with different spectral resolutions. For the lower spectral resolution STELLA data, we apply a two-dimensional cross-correlation technique to compute the SB2 solution. The higher-resolution PEPSI spectra are disentangled using a median subtraction technique. While ultimately we obtain a spot-corrected orbital solution with both approaches, the use of these two techniques allows us to obtain even more accurate results for the system’s orbit and activity diagnostics.

#### 3.1.1. Two-dimensional cross-correlation

Considering the spectral resolution of the STELLA spectra, tracking the secondary star is possible using a model spectrum fitted to the observed spectra. For this purpose, we used two different MARCS template spectra with  $T_{\text{eff}}=4500$  K,  $\log g=3.0$  and  $[\text{Fe}/\text{H}]=-0.5$  for the primary star and  $5500$  K,  $4.0$ , and  $0.0$  for the secondary, respectively ([Gustafsson et al. 2008](#)). We convolved the template spectra, while setting  $v \sin i$  to  $15 \text{ km s}^{-1}$  for the primary and  $3 \text{ km s}^{-1}$  for the secondary. We then used a set of RV shifts between the templates to calculate the two-dimensional cross-correlation functions (2D-CCFs) for each velocity shift. The locations of the peak values of the one-dimensional projections of the 2D-CCF power spectrum indicate the different RV values of the two stars. These values are marked with blue circles along the orbital phase in Fig. 1 (filled for the primary star, open for the secondary). More details about this technique can be found in [Weber & Strassmeier \(2011\)](#).

#### 3.1.2. Median subtraction

The uniquely high resolution of the PEPSI spectra allows for easy detection of the secondary star. To this end, we arranged the observed spectra according to orbital phase and compiled the dynamic spectrum between  $4800\text{--}5400 \text{ \AA}$ , which is shown in the lower panel of Fig. 2. In the rest frame of the primary star, it is clearly visible how the lines of the secondary star shift according to the phase of the orbit. In order to separate the spectra of the two stars, we first prepared equally sampled time series composite spectra in the rest frame of the primary.

We then determined the median value of all observations for each wavelength value (essentially, therefore, the medians of the columns in the lower panel of Fig. 2). This resulted in a single one-dimensional median composite spectrum. As a next step, we subtracted the median composite spectrum from each observed composite spectrum. This allowed us to obtain the spectrum of the secondary star for each observation time, taking into account the intrinsic variability of the primary star’s activity. Considering the orbital velocity corrections, as a final step we averaged these median subtracted spectra, thus obtaining the averaged (“mean”) spectrum of the secondary star. This spectrum is shown in Fig. B.1 with a template spectrum of the secondary star. This technique for disentangling the stellar spectra has the advantage of being model-independent, or that it preserves the line depth ratio of the stars.

#### 3.2. Further RV analysis

During the disentangling process, we obtained the RV values of both stars. However, in order to track the activity changes of the primary star on the RV curve, we performed the following steps. From all observed spectra, we subtracted the mean secondary spectrum, shifted by the corresponding RV values for each observation time. Thus, we obtained the spectrum of the primary star for each observing day. The RV values of the primary star HR 7275a were calculated by cross-correlating these spectra with the MARCS template spectrum assuming  $T_{\text{eff}}=4500$  K,  $\log g=3.0$ ,  $[\text{Fe}/\text{H}]=-0.5$  and  $v \sin i$  broadening of  $16 \text{ km s}^{-1}$ .

At this stage we must take into account the zero-point offset between the STELLA-SES and PEPSI instruments. [Strassmeier et al. \(2023\)](#) found the SES-minus-PEPSI grand mean RV difference to be  $-395\pm209 \text{ m s}^{-1}$ . [Adebali et al. \(2025\)](#) found this difference to be  $-180 \text{ m s}^{-1}$  for the RS CVn system  $\lambda$  And. In this paper, we obtained the same difference of  $-180 \text{ m s}^{-1}$  for

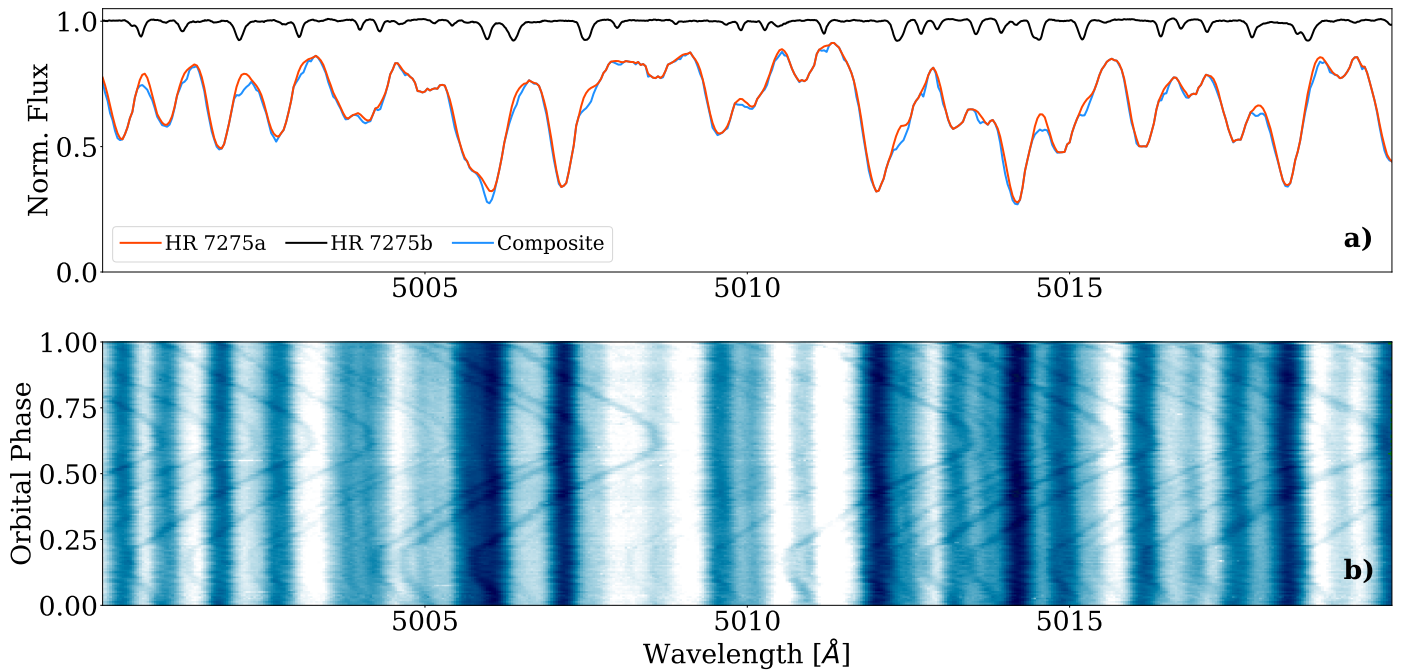


**Fig. 2.** Spectral disentangling by median subtraction. Panel *a*: The mean spectrum of the secondary star is plotted as a black line (top). The composite spectrum (blue) and a spectrum of the primary star (red) are plotted with a vertical shift of 0.15 at orbital phase 0.82. Panel *b*: Time series composite spectra phase folded with the orbital period.

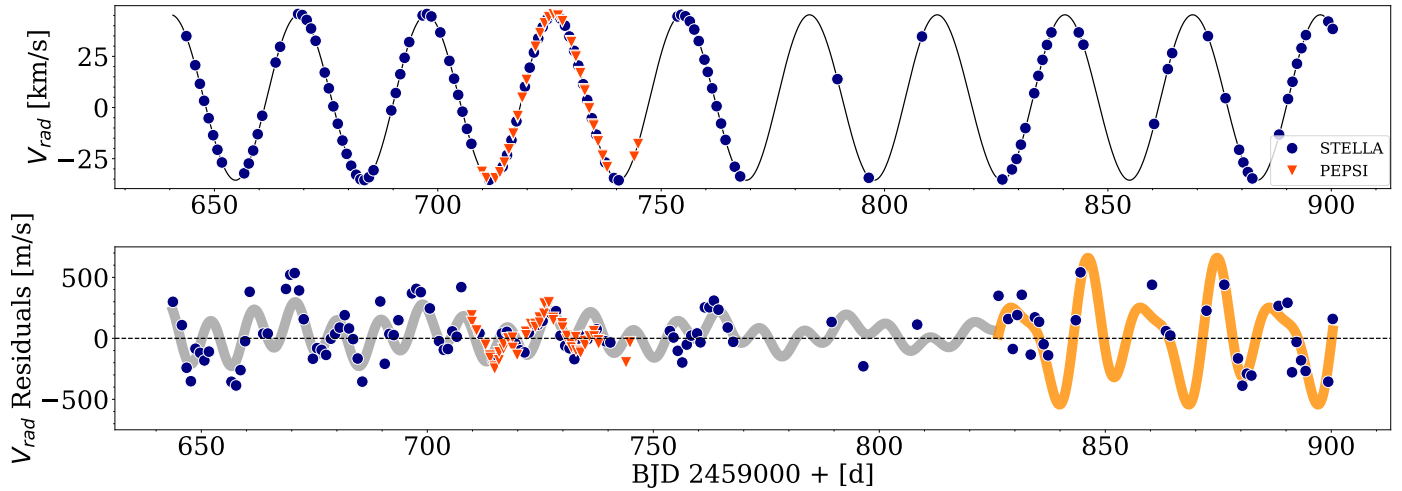


**Fig. 3.** Radial velocities of HR 7275a from VATT+PEPSI and STELLA+SES. In the upper panel, panel *a*, the SB1 orbital fit is plotted as a black line along with the data. STELLA+SES observations are indicated with dark blue circles; VATT+PEPSI observations are plotted in red triangles. In panel *b* the RV residuals are shown after removing the predicted orbital velocities. The RV jitter appears multi-peaked per rotation. The thick grey and orange lines emphasize two different rotational modulation models.

HR 7275 by taking the difference of the mean values for this observing window, with which we corrected the SES RV values to match PEPSI. We note that the PEPSI data for  $\lambda$  And and HR 7275 were obtained during the same nights close in time and are expected to be practically equal. Its uncertainty is estimated from the minimization of the rms of the orbital SB1 fit to be at most  $137 \text{ m s}^{-1}$ .

Since STELLA is a robotic telescope, observations were made every night according to the scheduled time, but some of the spectra had low S/N due to unfavorable weather conditions. Therefore, to eliminate outliers in the RV data set, a  $3\sigma$  clipping was applied (14 low-S/N spectra were removed). The resulting high-quality RV data were used in the following.

### 3.3. Spot correction

One of the major challenges for stars with large cool spots is determining the RV jitter caused by these dark features, which distort the observed spectra. Depending on the size of the starspot and its location on the stellar disk, the spot blocks the incident light beam and shifts the core of the spectral line. If the spot is located on the approaching half of the stellar disk, it blocks the light in such a way that a net redshift is observed, but if it is located on the receding half, the lack of light causes a net blueshift (see [Menuier 2023](#)). These modulations produce a sinusoidal shape, which was modeled by [Saar & Donahue \(1997\)](#) to quantify their effect on the RV curve. More complex models and observations have also been performed to obtain very accu-

**Table 1.** Orbital elements for HR 7275

Parameter	SB2 solution, spot-corrected	SB1 solution, spot-corrected	de Medeiros & Udry (1999)	Osten & Saar (1998)
$P_{\text{orb}}$ [d]	$28.586019 \pm 0.000015$	$28.5903 \pm 0.0004$	$28.58973 \pm 0.00002$	
$K_1$ [km s $^{-1}$ ]	$40.485 \pm 0.006$	$40.428 \pm 0.003$	$40.74 \pm 0.16$	$40.15 \pm 0.01$
$K_2$ [km s $^{-1}$ ]	$44.715 \pm 0.029$	...	$45.05 \pm 0.69$	$45.82 \pm 0.01$
$\gamma$ [km s $^{-1}$ ]	$4.902 \pm 0.012$	$5.202 \pm 0.005$	$4.11 \pm 0.14$	$5.97 \pm 0.19$
$T_0$ (BJD)	$2459773.74 \pm 0.12$	$2461403.02 \pm 0.08$	$2448976.78 \pm 0.05$	$2431043.908 \pm 0.01$
$e$	$0.005 \pm 0.001$	$0.0105 \pm 0.0007$	$0.010 \pm 0.004$	0
$\omega_1$ [deg]	$239.46 \pm 3.25$	$368.57 \pm 1.52$	$0.00 \pm 31.27$	...
$\omega_2$ [deg]	$59.46 \pm 3.25$	...	...	...
$a_1 \sin i$ [Mkm]	$15.933 \pm 0.023$	$15.890 \pm 0.011$	$16.016 \pm 0.064$	$15.784 \pm 0.004$
$a_2 \sin i$ [Mkm]	$17.545 \pm 0.021$	...	...	$18.014 \pm 0.004$
$M_1 \sin^3 i$ [ $M_{\odot}$ ]	$0.9585 \pm 0.0029$	...	$0.9843 \pm 0.0247$	$1.0070 \pm 0.0001$
$M_2 \sin^3 i$ [ $M_{\odot}$ ]	$0.8702 \pm 0.0028$	...	$0.8901 \pm 0.0186$	$0.8823 \pm 0.0001$
No. of obs.	176	176	28	28
Error of obs. of unit weight [km s $^{-1}$ ]	0.490	0.137	0.673	...

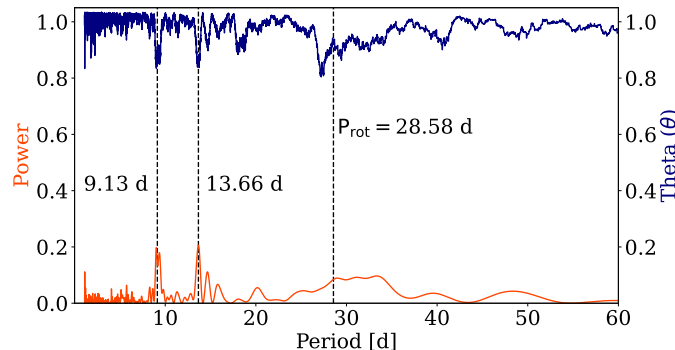


**Fig. 4.** Lomb-Scargle periodogram (red) of RV residuals from Fig. 3. The strongest peak appears at the half rotation of the star. Also one third of the rotation appears prominently as the second strongest peak in the periodogram. Phase dispersion minimization (PDM) is shown in blue which shows the strongest peak at 27.2 days.

rate RV observations for the detection of exoplanets or long-term activity modulations on the surface of stars (e.g., Boisse et al. 2011; Zhao & Dumusque 2023; Adebali et al. 2025).

HR 7275a is very active not only compared to the Sun, but also compared to similar types of active stars, such as  $\lambda$  And that we recently studied (Adebali et al. 2025). Because of the large starspots, it is easier to track the spot-related modulations in its RV curve than for stars with smaller spots. Therefore, to track the effect of spots, we obtained an SB1 orbital solution for the primary from approximately nine orbital revolutions of RV data as shown in Fig. 3. The resulting observed-minus-calculated ( $O - C$ ) residuals are shown in the bottom panel of the figure. The RV modulation depicted on the  $O - C$  curve shows a complex modulation during the time scale of  $\approx 250$  d. We see two trends with a separation by an observing gap of about 60 days (two stellar rotations): an epoch of lower jitter followed by an epoch of twice as large jitter. To model these two different amplitudes, we fitted three-sine functions with a small period shift which is typically caused by residual spot migration in latitude due to differential surface rotation. This is introduced as a time-dependent period shift with a calculated maximum of  $\sim 2$  days

during our observation window. The first global behavior is indicated in the bottom panel of Fig. 3 with a gray thick line between BJD 2,459,640-828. During this observing window, we calculated a RV modulation of up to  $320$  m s $^{-1}$  with the stellar rotation period of  $28.58 \pm 1.3$  d was seen (e.g., Fried et al. 1982; Strassmeier et al. 1989). The periodicity clearly indicates a global cause of the activity-induced RV variability. The second behavior between BJD 2,459,828-900 is indicated in the bottom panel of Fig. 3 with a thick orange line and modeled in the same way. Although the data points are distributed more sparsely, we still detect the same period of  $28.62 \pm 1.9$  d but with a much higher RV amplitude for the second global behavior with value of  $650$  m s $^{-1}$ . Both calculations are done with the minimum  $\chi^2$  approach of `scipy` package (Virtanen et al. 2020). To remove these spot effects from the final RV model, we subtract these fitted residual functions from the observed RV data.

Figure 4 shows the Lomb-Scargle periodogram of the fitted RV residuals, indicating the strongest peak at exactly half the rotation period. Another peak is found at one-third of the stellar rotation. However, this phenomenon is not unusual for stars with multiple spot configurations (see e.g., Boisse et al. 2011; Adebali et al. 2025) and can be seen not only in RV residuals but also in photometric modulations (e.g., Kővári et al. 2013).

### 3.4. Spot-corrected orbital solutions

We use both SB1 and SB2 configurations for our orbital solutions. For the eccentric anomaly in both configurations, we follow the recipe published by Danby & Burkardt (1983). For the Keplerian orbit fitting, we used the Python-`scipy` implementation of a least-square algorithm. The procedure is the following: We first determined an SB1 orbit using all available data from Young (1944), Eker (1989) and Osten & Saar (1998), spanning over 80 years. From this calculation, we kept only the orbital period and then fixed this value. This was followed by determining an SB2 solution. We then also calculated a spot-corrected SB1 orbit for the primary. The final spot-corrected solutions are listed in Table 1, along with the best solutions taken from the literature. HR 7275 exhibits a stable, synchronized, and nearly circular orbital configuration. We note that although the secondary star may

also have spots, their effect is essentially negligible compared to that of the K2IV-III primary due to the difference in brightness and the star's low  $v \sin i$  of  $\approx 1.2 \text{ km s}^{-1}$ . We thus did not calculate a spot correction for the secondary.

Our initial spot-uncorrected SB2 solution already gave significantly better fits than the most recent orbital calculation by [de Medeiros & Udry \(1999\)](#). After spot correction, the error for an observation of unit weight decreased further from  $0.51 \text{ km s}^{-1}$  to  $0.49 \text{ km s}^{-1}$  for the SB2 solution, and from 0.22 to 0.14 for the SB1 solution. The errors of the orbital elements on average decreased by almost a factor ten compared to [de Medeiros & Udry \(1999\)](#) which favored a marginal non-circular orbit with a low eccentricity of  $0.005 \pm 0.001$ . Although the surface spots of HR 7275a change slowly with each rotation, the spot correction still allows an orbital solution for the primary alone. It is more than twice as accurate as the SB2 solution due to the more precise RV measurements for the primary with respect to the faint secondary and is also listed in Table 1.

## 4. Doppler imaging

### 4.1. Data input and code summary

The surface map of HR 7275a is reconstructed using the *iMAP* code ([Carroll et al. 2012](#)), employing a multi-line inversion approach based on an average spectral line constructed from more than 500 individual lines with line depths exceeding 60 % of the continuum. The rotational line broadening of  $15.4 \text{ km s}^{-1}$  of HR 7275a makes it a difficult but possible Doppler imaging (DI) target. Atomic data for the multi-line inversion are drawn from the Vienna Atomic Line Database VALD-3 ([Ryabchikova et al. 2015](#)), covering the  $4800\text{--}5400 \text{ \AA}$  wavelength range of our PEPSI CD III spectra. We preferred the  $4800\text{--}5400 \text{ \AA}$  range for DI because we have CD III exposures for every observing night and thus the best phase coverage when compared to the red CDs. The (pseudo) average spectral line is computed using a Singular Value Decomposition (SVD) algorithm, where the dimensionality (rank) of the signal subspace was determined via a bootstrap-permutation test (see [Carroll et al. 2012](#), for details). Noise estimates are similarly obtained from the bootstrap procedure. This methodology results in weighted mean line profiles with typical S/N of approximately 20,000 per pixel, substantially higher than the  $\approx 400\text{--}900$  S/N per pixel achieved for the individual spectra.

The high resolving power of the PEPSI spectra ( $R \approx 250,000$ ; corresponding to  $1.2 \text{ km s}^{-1}$  or  $0.024 \text{ \AA}$  at  $6000 \text{ \AA}$ ), in combination with the mean full width of the spectral lines at continuum level ( $2 \lambda/c v \sin i \approx 0.6 \text{ \AA}$ ), provides 25 resolution elements across the projected stellar disk. Following the simulations by [Piskunov & Wehlau \(1990\)](#), which suggest that at least five resolution elements are required for successful DI, the PEPSI data are properly dimensioned for surface reconstruction. In contrast, the lower resolving power of STELLA+SES spectra ( $R=55,000$ ) renders them a border case for DI in this case.

The computation of local line profiles within *iMAP* involves solving the radiative transfer equation for each surface pixel across 72 depth points, using a grid of tabulated Kurucz ATLAS-9 model atmospheres ([Kurucz 1993; Castelli & Kurucz 2003](#)). The local line profiles are calculated under the assumption of one-dimensional (1D) geometry and local thermodynamic equilibrium (LTE). The atmospheric grid spans effective temperatures from  $3500 \text{ K}$  to  $8000 \text{ K}$  in increments of  $250 \text{ K}$ , interpolated to match the stellar surface gravity, metallicity, and micro-turbulence parameters obtained from global spectrum synthesis.

The stellar surface is divided into  $5^\circ \times 5^\circ$  elements, corresponding to a grid of  $72 \times 36$  pixels and totaling 2592 surface segments. A stellar inclination of  $56^\circ$ , which is calculated by using the stellar parameters obtained from the literature and ParSES results. The surface reconstruction employs an iteratively regularized Landweber method, implementing a fixed-point iteration scheme designed to minimize the sum of the squared residuals. The method takes the noise level of the data set as a fixed-point and stops the iteration when the sum of the squared residuals reaches the noise limit. In other words, this iteration technique is in a way in the opposite direction when compared with other methods such as Tikhonov or Maximum Entropy, where the noise level is used as an additional term to the  $\chi^2$  while applying the iteration (see [Carroll et al. 2012](#), and references therein). Our final image has been achieved with a  $\chi^2$  of 0.005.

### 4.2. Adopted stellar parameters

As we disentangled both spectra, stellar parameters are obtained for both stars. For the photospheric parameters, we compared the SES spectra with synthetic templates. Our code Parameters-from-SES (ParSES; [Allende Prieto \(2004\); Jovanovic et al. \(2013\)](#)) is a software package which employs a grid of pre-computed model spectra generated with Turbospectrum ([Plez 2012](#)) and a line list obtained from VALD-3 ([Ryabchikova et al. 2015](#)). ParSES selects the best-fit to the observed spectra based on the minimum distance method with a non-linear-simplex optimization ([Allende Prieto et al. 2006](#)). We applied this procedure to 122 STELLA spectra observed during a time coverage of 260 days for the primary star. ParSES provided in total five stellar parameters: effective temperature  $T_{\text{eff}}$ , projected rotational velocity  $v \sin i$ , microturbulence  $\xi_t$ , gravity  $\log g$ , and metallicity [M/H]. The calculated values for those parameters are as follows;  $T_{\text{eff}}=4480 \pm 70 \text{ K}$ ,  $v \sin i=15.4 \pm 1.2 \text{ km s}^{-1}$ ,  $\xi_t=2.0 \pm 0.2 \text{ km s}^{-1}$ ,  $\log g=2.8 \pm 0.2$ , and  $[\text{M/H}]=-0.19 \pm 0.10$ . Errors are assumed from the  $1\sigma$  rms values from the 122 individual spectra. Our  $v \sin i$  and  $\xi_t$  values agree with the one previously computed by [Osten & Saar \(1998\)](#). [Strassmeier et al. \(1989\)](#) showed that the visual magnitude change of HR 7275 has a varying amplitude from 0.002 to 0.2 mag. This change already affects the determination of  $T_{\text{eff}}$  by  $\approx 230 \text{ K}$ . At least for the time range of our observations, those values are similar to the values calculated by [O'Neal et al. \(1996\)](#) and [Osten & Saar \(1998\)](#). By using the parallax from [Gaia Collaboration et al. \(2023\)](#), we calculate a luminosity of  $30.6 \pm 2.8 L_{\odot}$  based on  $V=5.893 \text{ mag}$ ,  $A_V=0$ , and a bolometric correction of  $-0.48$  from [Popper \(1980\)](#). The Stefan-Boltzmann law then suggests a likely radius of  $9.2 R_{\odot}$  (primary component). Combining the ParSES value for  $\log g$  and this radius gives a likely mass for the primary star of  $1.93 \pm 0.45 M_{\odot}$ . By using this formal mass, we estimate a most-likely inclination of  $\approx 52^\circ$ .

Prior to the iterative Doppler-imaging process, we run several test solutions with different inclinations of the rotational axis  $i$  (of the primary). Solutions in five-degree steps from  $i = 20^\circ$  to  $i = 70^\circ$  and with a fixed  $v \sin i$  provide a best fit at  $i = 50^\circ$  as judged from the minimum of the achieved  $\chi^2$  with an equally likely range of approximately  $\pm 7^\circ$ . This value agrees very well with the above determination of the inclination of the system. If we assume that the rotational axis of the primary is perpendicular to the orbital plane, then we can use this inclination also for the orbital elements and obtain real masses.

Because our Doppler imaging assumes a perfectly spherical star, we have estimated the oblateness of the primary due to tidal forces or rapid rotation based on our orbit in Table 1, the stellar

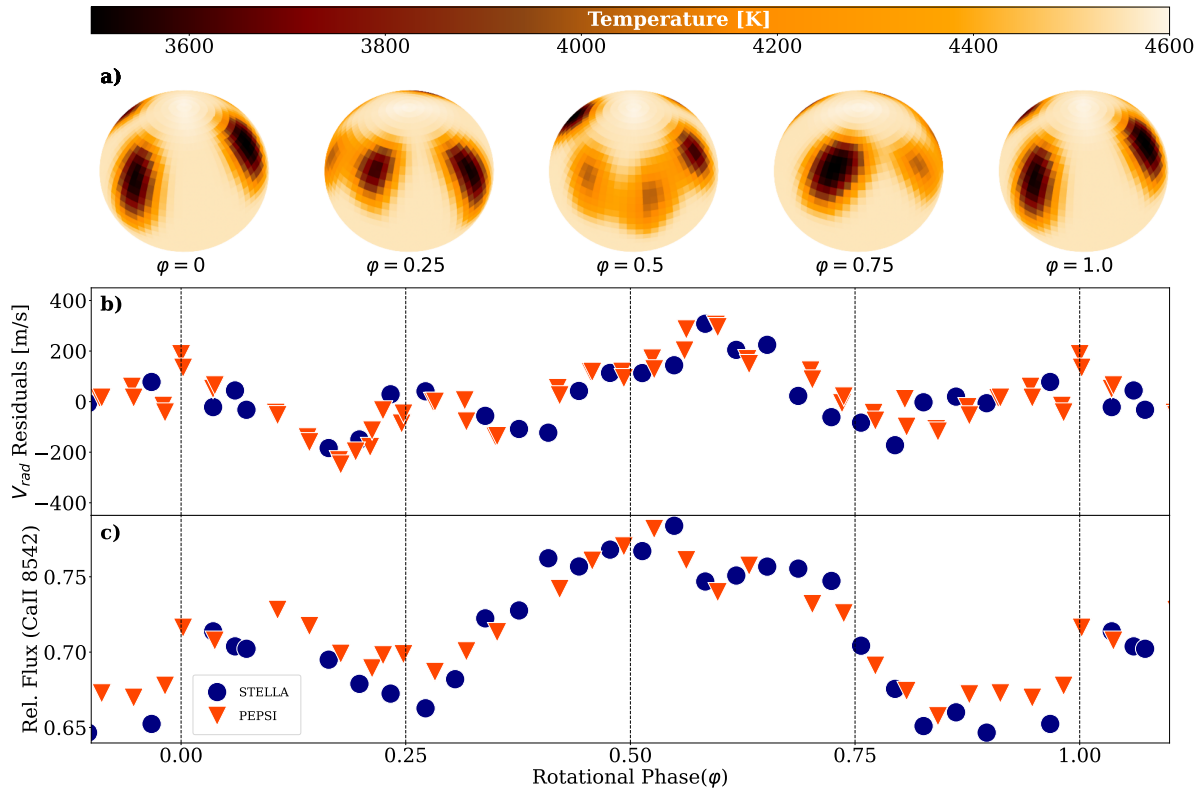


**Fig. 5.** Panel *a*: Doppler image of HR 7275a. The rotational phases are indicated via phase  $\varphi$  with a sampling of 0.25. Panel *b*: Contemporaneous RV modulation due to the spot modulation. Panel *c*: Relative flux modulation of Ca II IRT 8542 Å simultaneous to the DI. Dark blue dots show the STELLA data set and red triangles indicate the PEPSI observations.

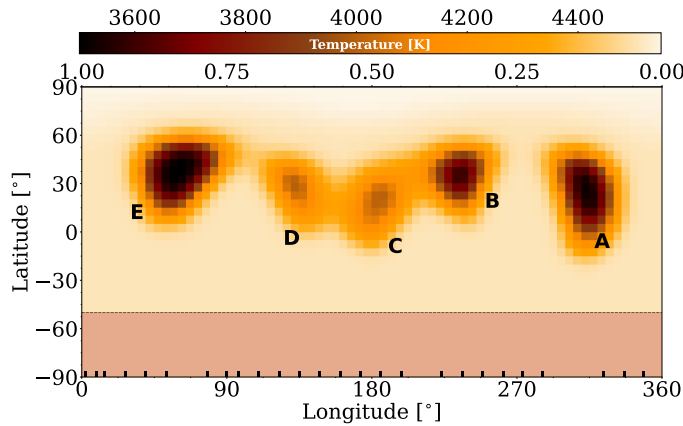


**Fig. 6.** Mercator map of the spotted surface of HR 7275a.

parameters in Table 2, and a range of Love numbers following Leconte et al. (2011). The range for the expected polar-to-point radii never exceeded 0.38–1.4 %. This verifies that our spherical-shape assumption is a reasonably good representation as the star does not experience significant elongation.

We also calculate stellar parameters for the secondary star using ParSES. For this, we employ a disentangled PEPSI spectrum of the secondary star (shown in the Appendix in Fig. B.1) obtained via the median-subtraction method explained above. The stellar parameters for the secondary star were obtained as follows;  $T_{\text{eff}}=5530\pm116$  K,  $v \sin i=1.4\pm0.3$  km s $^{-1}$ ,

**Table 2.** Stellar parameters obtained in this paper.

Parameters	Primary	Secondary
$T_{\text{eff}}$ [K]	$4480\pm70$	$5530\pm116$
$\log g$ (cgs)	$2.8\pm0.3$	$4.0\pm0.2$
$v \sin i$ [km s $^{-1}$ ]	$15.4\pm1.2$	$1.4\pm0.3$
$\xi_t$ [km s $^{-1}$ ]	$2.0\pm0.2$	$0.8\pm0.2$
[M/H]	$-0.19\pm0.10$	$-0.18\pm0.11$
$P_{\text{rot}}$ [d]	$=P_{\text{orb}}$	...
$i$ [°]	$52\pm8$	...
$M$ [ $M_{\odot}$ ]	$1.93\pm0.45$	$1.75\pm0.48$
A(Li)	$0.58\pm0.1$	$0.16^{+0.23}_{-0.63}$
MK class <sup>1</sup>	K2 IV-III	G4 V-IV

Notes. <sup>1</sup>Based on above  $\log g$  and  $T_{\text{eff}}$  and the tables in Gray (2022).

$\xi_t=0.8\pm0.2$  km s $^{-1}$ ,  $\log g=4.0\pm0.2$ , and [M/H]= $-0.18\pm0.11$ . The stellar parameters for both stars are summarized in Table 2. Because we have an SB2 orbital solution, we find the secondary mass to be  $1.75\pm0.48 M_{\odot}$ .

#### 4.3. Doppler imaging results

The spot configuration of HR 7275a at the time of our observations in May-June 2022 is shown in Fig. 5. The image has been obtained from a single rotation of the star and is presented via

**Table 3.** Spots on HR 7275a in May-June 2022.

Spot ID	Long (°)	Lat (°)	$\Delta T_{\text{spot}}$ (K)	Area (%)
A (umbra)	315	25	1000	14
A (penumbra)			350	6
B (umbra)	235	35	900	8
B (penumbra)			300	7
C	185	20	500	14
D	135	30	500	12
E (umbra)	60	35	1000	13
E (penumbra)			450	6

**Notes.** Longitudes and latitudes are given for the spot center. The spot temperature difference is given for the coolest part of the spot. Three spots show possibly umbral and penumbral features (A, B and E). The spot area is given in per cent of the visible hemisphere.

**Table 4.** Logarithmic absolute emission-line fluxes in  $\text{erg cm}^{-2}\text{s}^{-1}$  for HR 7275.

Bandpass	Continuum flux (per Å)	Average line flux	Average variability amplitude	Fit rms
Ca II H	6.2060	6.135	0.571	0.056
Ca II K	6.2060	6.247	0.732	0.084
H $\alpha$	6.4462	6.026	0.296	0.033
Ca II 8542	6.3911	6.154	0.141	0.013

**Notes.** Variability amplitude and fit rms of relative fluxes in units of the continuum (= 1)

an orthographic projection with four equally-spaced rotational phases. Figure 6 shows the same image in a pseudo-Mercator projection for a more global view of the stellar surface. We did not reconstruct a cool (dark) polar spot. Instead, we see a weakly warmer (bright) region about 100 K warmer than the quiet surface of HR 7275a. It is likely unreal because the expected temperature uncertainty in the reconstruction is about 100 K, mostly due to the (comparably) low rotational line broadening but also the remaining uncertainties due to our LTE assumption.

We observed in total five cool spots that appear separated in longitude on average 60° from each other. The spot locations, temperature differences, and surface coverages compared with the visible stellar surface are quantified and given in Table 3. Among those five spots, three (denoted A, B and E) show possibly a solar-like umbral and penumbral structure with an umbral spot temperature difference  $\Delta T$  of  $\approx 1000$  K cooler than the quiet stellar photosphere. The spots named C and D appear significantly warmer than spots A, B, and E, with  $\Delta T$  of  $\approx 500$  K relative to the photosphere. Both are located close-together in the same region on the stellar surface at the phase of quadrature at  $\approx 0.6$ , that is, in the trailing hemisphere 90° behind the binary's apsidal line.

## 5. Magnetic activity and lithium abundance

### 5.1. Ca II H&K, H $\alpha$ and Ca II IRT 8542 Å line-core emissions

Four chromospheric activity indicators are being used in this paper: Ca II H&K, H $\alpha$ , and one of the infrared triplet lines Ca II IRT (8542 Å). As shown in Fig. B.3, these diagnostics are available

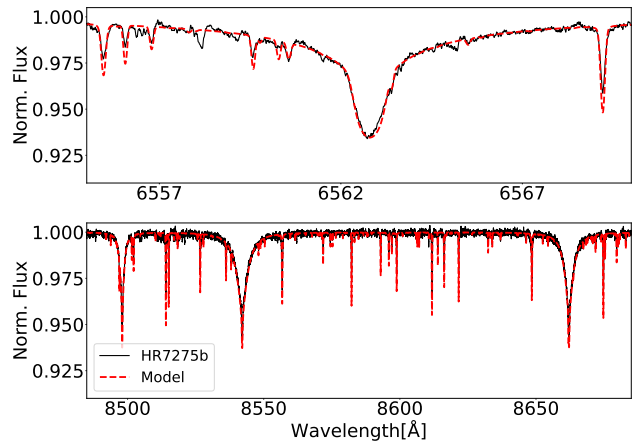


**Fig. 7.** Disentangled spectrum of HR7275b near H $\alpha$  (upper panel) and Ca II IRT region (lower panel). The observed spectrum is indicated by a black line and the model is indicated by dashed red line.

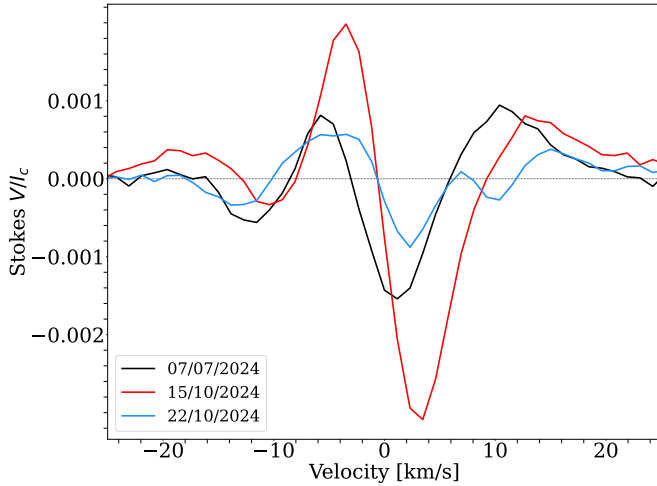
for a total of six rotations; four consecutive stellar rotations are within the  $BJD$  2,459,653-766 window, while another two consecutive rotations are tracked between 2,459,824 and 2,459,882.

We measure the relative flux in a bandwidth of one Å centered on the line core of 3968.5 Å and 3933.7 Å for Ca II H&K, 8542.1 Å for Ca II IRT and 6562.8 Å for H $\alpha$ . For the latter two lines, we have spectra from both STELLA and PEPSI while the Ca II H&K analysis is done only with STELLA data (PEPSI+VATT spectra did not cover the bluest wavelength regions due to the long fiber). The surface temperature calculations are based on ParSES as explained in Sect. 4.2. The fluxes for H $\alpha$  and Ca II IRT are computed after the disentangling for the corresponding wavelength regions. The obtained secondary star spectrum for H $\alpha$  and Ca II IRT regions are shown in Fig. 7. Because our disentangling processes fail for the Ca II H&K region mostly because of too low S/N and the intrinsic variability of the primary, we calculated Ca II H&K line fluxes from the composite spectra. We note that the relative contribution of the secondary must be rather small at this wavelength region. The reason for this is that the  $v \sin i$  of the secondary component is very small, thus the secondary star is not expected to be very active. In addition, as a nature of the RS CVn systems, the strong line emissions of the primary star are expected to dilute the signatures coming from the companion.

Before the conversion to absolute flux, we match the continuum settings of STELLA spectra with that from PEPSI spectra because of the latter superiority in quality and data reduction (see Järvinen & Strassmeier 2025). Intrinsic flux-variability amplitudes are determined by three sinusoidal fits for each of the four consecutive stellar rotation. The average amplitude of the chromospheric (flux) variability and its rms values with respect to these fits are given in Table 4.

The chromospheric activity of HR 7275 appears strongly modulated with either the rotational period ( $\approx 28$  d) or half of it ( $\approx 14$  d) depending upon its single- or a double-humped appearance (see Table A.3). As shown in the Appendix in Fig. B.3, the maximum amplitude change is about 35% for Ca II H&K and Ca II IRT 8542 Å, while it is 40% for H $\alpha$ . The peak-amplitude location of these emissions appears at shifts of about 0.1 phases per rotation, despite that the overall activity modulation appears stable during the first four rotations. During the third of the covered six full stellar rotations, that is the time of our photospheric

a.



b.

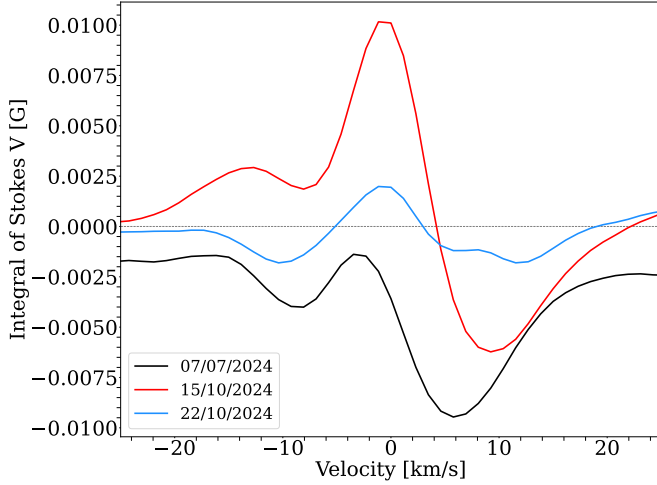


**Fig. 8.** Stokes-V based magnetic field measurements for HR 7275 from 2024. *a.* LSD line profiles from PEPSI in units of normalized intensity. *b.* Integrated Stokes-V profiles in units of Gauss.

Doppler imaging, we observe a complex double-peaked flux distribution with the strongest peak at approximately phase 0.55 (Fig. 5c), which coincides with the position of the two weakest (warmest) spots D and C during their central-meridian passage. The two-times weaker secondary peak appears around phase 0.15 and coincides with the central-meridian passage of the large spot A. Both peaks appear similarly in the other three chromospheric tracers. The main peak at phase 0.55 is particularly prominent in H $\alpha$  which is indicative of a facular origin, or at least contribution, compared to solar analogy.

## 5.2. Magnetic field measurements

We obtained magnetic field measurements from three PEPSI Stokes-V spectra in 2024. The spectra cover the wavelength range from 4800  $\text{\AA}$  to 5441  $\text{\AA}$  and are converted to Least Squares Deconvolution (LSD; e.g. [Donati et al. 1997](#)) line profiles built from the most recent line list from VALD-3 ([Ryabchikova et al. 2015](#)). For the magnetic field measurement, we implemented the prescription from [Kochukhov et al. \(2010\)](#) based on the method of [Solanki & Stenflo \(1984\)](#). The three LSD profiles are shown in Fig. 8a.

The disk-integrated longitudinal magnetic field was  $-15.2 \pm 2.7$  G for the one spectrum from July 2024. For the two

**Table 5.** Magnetic field measurements for HR 7275.

BJD	Phase ( $\varphi$ )	$B_{\text{long}}$ [G]	$ B $ [G]
2,460,498.973	0.611	$-15.2 \pm 2.7$	$57.1 \pm 0.7$
2,460,598.588	0.097	$+0.6 \pm 2.0$	$35.2 \pm 0.7$
2,460,605.686	0.345	$-14.0 \pm 2.6$	$17.8 \pm 0.6$

observations in October 2024, seven days apart, we obtained rather divergent results of  $+0.6 \pm 2.0$  G and  $-14.0 \pm 2.6$  G. While we can not conclude on the global morphology of the field from these three measurements, it indicates the presence and phase dominance of even and odd polarities coexisting within short (phase) distances on the surface.

## 5.3. Lithium abundance

In order to get an estimate for the mixing inside the star, we determine the logarithmic lithium abundance, A(Li), of the primary and also attempt to measure it for the secondary star. After disentangling the spectra within the region between 6300-7400  $\text{\AA}$ , using the median subtraction technique explained in Sect. 3.1.2, we first built a median spectrum from all 26 PEPSI spectra of the primary and the secondary star. These two steps, disentangling and phase averaging, enabled not only the removal of the respective binary spectrum but also identified and removed the telluric contamination. This single spectrum is of high quality with a median S/N per pixel of 300:1 for the primary and 99:1 for the secondary.

We then employed the line-synthesis program Turbospectrum ([Plez 2012](#)) together with the fitting routine TurboMPfit ([Steffen et al. 2015](#)) and the line list from [Meléndez et al. \(2012\)](#). Many different fits were obtained for the primary by both including and excluding TiO lines, fixed and adapted continuum level, line shifts, and macroturbulence broadening. Somewhat surprisingly, we found that the impact of TiO molecular lines is very moderate despite the low  $T_{\text{eff}}$  of 4480 K. Presumably, this can be explained by the lower particle densities in the line formation regions of this giant star at  $\log g=2.8$ . Figure 9a shows the best fit with an abundance of  $0.58 \pm 0.1$ , with or without TiO blends. The comparably large error,  $\pm 0.1$  dex, is by far due to the  $\pm 70$  K uncertainty of the ParSES-based  $T_{\text{eff}}$  rather than anything else. The internal fit quality of all our Turbospectrum runs was always around or even below 0.01 dex, thus a factor ten lower, as the fit is so much more sensitive to the overall photospheric effective temperature. In addition, the contribution of TiO lines does not affect the fit significantly, both versions result in abundances less than 1% different. Although HR 7275a displays spots cooler than the surrounding photosphere by 1000 K, a fact which should favor local TiO line formation, the effective temperature of the star is just too high to allow the detection of these lines ([Strassmeier & Steffen 2022](#)). Similar observations and conclusion were reported by [Adebali et al. \(2025\)](#) for  $\lambda$  And, which is only about 100 K hotter than HR 7275a.

A similar procedure than above was applied to the secondary spectrum with the difference that we adopted the continuum at 6708  $\text{\AA}$  as a free parameter from the beginning on and fixed line shift and total line broadening. This left only the continuum and the Li abundance as free parameters. The reason is simply the comparable low S/N. Fits were obtained for three effective temperatures,  $\pm 115$  K around the nominal  $T_{\text{eff}}$  of 5530 K, and three relative metallicities 0,  $-0.1$ , and  $-0.2$ . The best fit was obtained

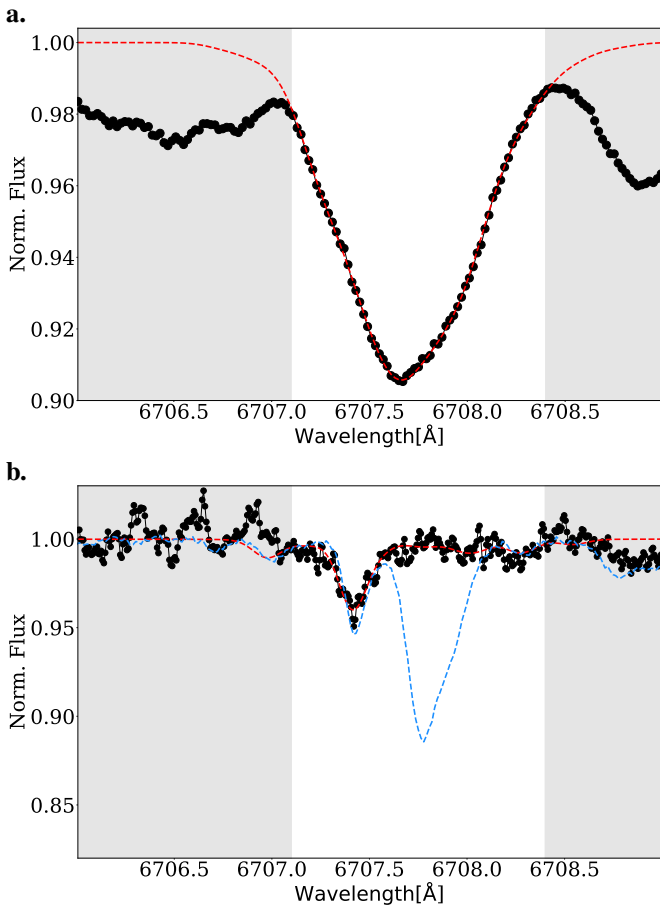


**Fig. 9.** Lithium abundance analysis. Panel *a*: Median spectrum of HR 7275a (black dots) and Turbospectrum fit (dashed red line). The gray shaded areas indicate the regions outside the fitting range (in white). Panel *b*: Same plot for HR 7275b. The blue dashed line shows a PEPSI spectrum of 70 Vir.

for  $T_{\text{eff}}=5530$  K and  $[\text{Fe}/\text{H}]=-0.1$  with  $A(\text{Li})=0.16$  dex and is shown in Fig. 9b. Its internal error is more or less meaningless but we estimate a real error from the range of  $\pm 115$  K in temperature and  $\pm 0.1$  dex in metallicity, which then suggests only a marginal detection of lithium of  $A(\text{Li})=+0.16^{+0.23}_{-0.63}$ . The final result for the lithium abundance of the primary is very robust,  $A(\text{Li})=0.58\pm 0.1$  dex, indicating considerable mixing as expected for an evolved star. The  ${}^6\text{Li}/\text{Li}$  isotopic ratio cannot be deduced from the highly broadened spectrum and was fixed at 0.0. The lithium abundance of the secondary seems to be extremely low. For comparison,  $A(\text{Li})=1.12$  for the single benchmark star 70 Vir (also classified as G4 V-IV), so roughly a factor 10 higher than for HR7275b.

## 6. Summary and conclusions

In this paper, we used different techniques to understand the activity behavior of the primary star of the system HR 7275. We developed a python tool called DISTRACT using two different methods for isolating the spectra of two stars. This enabled us to quantify the following activity indicators for HR 7275a.

The average RV jitter of HR 7275a is comparable to what has been observed for the highly asynchronous primary star in the  $\lambda$  And system (Adebali et al. 2025). The RV contribution from HR 7275a spots have two different global modulation behavior. The first modulation pattern causes up to  $320 \text{ m s}^{-1}$  of

RV jitter and the second global modulation peaks at  $650 \text{ m s}^{-1}$ . Our global fits for these modulations gives an estimate for the general activity behavior of the star. Nevertheless, the activity modulation differs further for each rotation of the star. Between BJD 2,459,640-2,459,828, we had four consecutive rotations with good enough sampling rate. During the first rotation, the RV modulation reaches up to  $600 \text{ m s}^{-1}$  but diminishes to  $200 \text{ m s}^{-1}$  in the next two rotations resulting in an average of  $320 \text{ m s}^{-1}$  when including the other two rotations. After BJD 2,459,828, we had two more but less-well sampled rotations. Both shows a larger spread in RV jitter than before and a higher jitter average of  $650 \text{ m s}^{-1}$ . The reason for this change is simply the disk asymmetry caused by the spot distribution with respect to each other and the stellar limb. This may be a feature that separates HR 7275a from its asynchronously rotating RS CVn cousin  $\lambda$  And, which shows a stable spot coverage, and thus stable RV jitter, during 522 d of observations (almost ten stellar rotations). In addition, the occurrence of three relatively large spots, each occupying almost 10% of the surface of HR 7275a, is indicative that the star has a more intense dynamo process than  $\lambda$  And. At this point, we must conclude that synchronized rotation does not necessarily favor more stable magnetic structures, and therefore a more stable stellar magnetic activity.

This aspect is also observed by chromospheric emissions. As shown in Fig. B.3, the activity peaks appear at different relative flux values. For Ca II H&K and Ca II IRT 8542 emissions, the highest activity appears during the second stellar rotation. Contrary to that, H $\alpha$  emission flux peaks at the third rotation where we also construct the Doppler image of the primary star. This shows that, emission fluxes in H $\alpha$  regime do not exactly follow the Ca II IRT and Ca II H&K. When we consider the formation height of those emission lines, we conclude that the more intense dynamo behavior affects different layers of the chromosphere with a varying impact.

Characterizing the activity jitter on RVs and confirming these effects with Doppler image gives a broader understanding for how starspot structure affects the chromospheric emissions. As shown in Fig. 5, relatively warmer spots cause a larger chromospheric emission on Ca II H&K. We interpret this as a faculae dominated region heats up the upper atmosphere more than we see above the cooler spots on HR 7275a. This effect is also observable in the Sun, where magnetic field is the main source of the heating mechanism in the chromosphere. The dominating spots marked with C and D appear also closer to each other than the other resolved spots. This may also enhance the emission more than the observed single spots (A and E), while they are passing from the central meridian.

Monitoring the surface activity allowed us to determine both SB1 and SB2 solutions for the system by correcting the activity “jitter”. These corrections allowed us to improve the orbital solution by 35% for the SB1 calculation and by about 5% for the SB2 calculation. The reason for the latter being relatively low is the fact that we cannot detect surface effects on RVs for the secondary star likely because of its very low  $v \sin i$  and the low relative activity signal appearing in the composite spectra. In the near future, we plan for a simultaneous RV and activity fit with different analysis techniques such as Gaussian processes (e.g., Aigrain & Foreman-Mackey 2023).

The improved orbit also enabled more accurate stellar parameters for both primary and secondary star. The most recent orbital calculations in the literature by de Medeiros & Udry (1999), suggested similar minimum masses for the primary as listed in Table 1. However, since there is no information provided

about the inclination by [de Medeiros & Udry \(1999\)](#), they could not provide values for the actual masses. Our best value for the primary mass is  $1.93 \pm 0.45 M_{\odot}$  based on an inclination of  $52 \pm 8^\circ$  from ParSES calculations. [Eker \(1989\)](#) suggested a mass range for the secondary star between  $0.9$ – $1.1 M_{\odot}$  by using their SB1 solution. When we combine our SB2 solution with the Stefan-Boltzmann equations, we found a consistent but much higher value of  $1.75 M_{\odot}$ .

Finally, we determined lithium abundances for both components of the system for the first time. The primary star has  $A(\text{Li})=0.58$  dex and the secondary star of  $A(\text{Li}) \approx 0.16$ . The latter being only a marginal detection. The comparably low abundance of the giant primary indicates that its photospheric abundance must have undergone significant mixing.

**Acknowledgements.** We thank an anonymous referee for the constructive and detailed comments that improved the quality of this article. This work is based partially on data obtained with the Stellar Activity-2 (STELLA-II) robotic telescope in Tenerife, an AIP facility jointly operated by AIP and IAC (<https://stella.aip.de/>) and partially on data from PEPSI acquired with the Large Binocular Telescope (LBT) and the Vatican Advanced Technology Telescope (VATT) (see <https://pepsi.aip.de/>). The LBT is an international collaboration among institutions in the United States, Italy and Germany. LBT Corporation partners are: The University of Arizona on behalf of the Arizona Board of Regents; Istituto Nazionale di Astrofisica, Italy; LBT Beteiligungsgesellschaft, Germany, representing the Max-Planck Society, The Leibniz Institute for Astrophysics Potsdam, and Heidelberg University; The Ohio State University, representing OSU, University of Notre Dame, University of Minnesota and University of Virginia. In this work, we heavily used python3 libraries: astropy ([Astropy Collaboration et al. 2013, 2018, 2022](#)), numpy ([Harris et al. 2020](#)) and scipy ([Virtanen et al. 2020](#)). The authors thank B. Seli from Konkoly Observatory for making available his Python code for spot segmentation (see [Kővári et al. 2024](#), Appendix F). ZsK acknowledges the financial support of the Hungarian National Research, Development and Innovation Office grant KKP-143986.

Ilyin, I. V. 2000, University of Oulu, Division of Astronomy  
 Järvinen, S. P. & Strassmeier, K. G. 2025, A&A, 698, A93  
 Jovanovic, M., Weber, M., & Allende Prieto, C. 2013, Publications de l’Observatoire Astronomique de Beograd, 92, 169  
 Kővári, Zs., Korhonen, H., Strassmeier, K. G., et al. 2013, A&A, 551, A2  
 Kővári, Zs., Strassmeier, K. G., Kriskovics, L., et al. 2024, A&A, 684, A94  
 Kochukhov, O., Makaganiuk, V., & Piskunov, N. 2010, A&A, 524, A5  
 Kriskovics, L., Vida, K., Kővári, Zs., Garcia-Alvarez, D., & Oláh, K. 2013, Astronomische Nachrichten, 334, 976  
 Kurucz, R. 1993, Robert Kurucz CD-ROM, 13  
 Leconte, J., Lai, D., & Chabrier, G. 2011, A&A, 528, A41  
 Meléndez, J., Bergemann, M., Cohen, J. G., et al. 2012, A&A, 543, A29  
 Menuier, N. 2023, in Star-Planet Interactions, ed. L. Bigot, J. Bouvier, Y. Lebreton, A. Chiavassa, & A. Lèbre, 22  
 Neff, J. E., O’Neal, D., & Saar, S. H. 1995, ApJ, 452, 879  
 O’Neal, D., Saar, S. H., & Neff, J. E. 1996, ApJ, 463, 766  
 Osten, R. A. & Saar, S. H. 1998, MNRAS, 295, 257  
 Piskunov, N. E. & Wehlau, W. H. 1990, A&A, 233, 497  
 Plez, B. 2012, Turbospectrum: Code for spectral synthesis, Astrophysics Source Code Library, record ascl:1205.004  
 Popper, D. M. 1980, ARA&A, 18, 115  
 Ryabchikova, T., Piskunov, N., Kurucz, R. L., et al. 2015, Phys. Scr, 90, 054005  
 Saar, S. H. & Donahue, R. A. 1997, ApJ, 485, 319  
 Sablowski, D. P., Järvinen, S., & Weber, M. 2019, A&A, 623, A31  
 Solanki, S. K. & Stenflo, J. O. 1984, A&A, 140, 185  
 Steffen, M., Prakapavičius, D., Caffau, E., et al. 2015, A&A, 583, A57  
 Strassmeier, K. G. 2009, A&A Rev., 17, 251  
 Strassmeier, K. G., Granzer, T., Weber, M., et al. 2004, Astronomische Nachrichten, 325, 527  
 Strassmeier, K. G., Hall, D. S., Boyd, L. J., & Genet, R. M. 1989, ApJS, 69, 141  
 Strassmeier, K. G., Hall, D. S., Fekel, F. C., & Scheck, M. 1993, A&AS, 100, 173  
 Strassmeier, K. G., Ilyin, I., Järvinen, A., et al. 2015, Astronomische Nachrichten, 336, 324  
 Strassmeier, K. G., Ilyin, I., & Steffen, M. 2018, A&A, 612, A44  
 Strassmeier, K. G., Kővári, Zs., Weber, M., & Granzer, T. 2024, Nature Communications, 15, 9986  
 Strassmeier, K. G. & Steffen, M. 2022, Astronomische Nachrichten, 343, e20220036  
 Strassmeier, K. G., Weber, M., Gruner, D., et al. 2023, A&A, 671, A7  
 Virtanen, P., Gommers, R., Oliphant, T. E., et al. 2020, Nature Methods, 17, 261  
 Vogt, S. S. & Penrod, G. D. 1983, PASP, 95, 565  
 Weber, M., Granzer, T., & Strassmeier, K. G. 2016, in Society of Photo-Optical Instrumentation Engineers (SPIE) Conference Series, Vol. 9910, Observatory Operations: Strategies, Processes, and Systems VI, ed. A. B. Peck, R. L. Seaman, & C. R. Benn, 99100N  
 Weber, M. & Strassmeier, K. G. 2011, A&A, 531, A89  
 Young, R. K. 1944, JRASC, 38, 366  
 Zhao, Y. & Dumusque, X. 2023, A&A, 671, A11

## References

Adebali, Ö., Strassmeier, K. G., Ilyin, I. V., et al. 2025, A&A, 695, A89  
 Aigrain, S. & Foreman-Mackey, D. 2023, ARA&A, 61, 329  
 Allende Prieto, C. 2004, Astronomische Nachrichten, 325, 604  
 Allende Prieto, C., Beers, T. C., Wilhelm, R., et al. 2006, ApJ, 636, 804  
 Astropy Collaboration, Price-Whelan, A. M., Lim, P. L., et al. 2022, ApJ, 935, 167  
 Astropy Collaboration, Price-Whelan, A. M., Sipőcz, B. M., et al. 2018, AJ, 156, 123  
 Astropy Collaboration, Robitaille, T. P., Tollerud, E. J., et al. 2013, A&A, 558, A33  
 Boisse, I., Bouchy, F., Hébrard, G., et al. 2011, A&A, 528, A4  
 Carroll, T. A., Strassmeier, K. G., Rice, J. B., & Künstler, A. 2012, A&A, 548, A95  
 Castelli, F. & Kurucz, R. L. 2003, in Modelling of Stellar Atmospheres, ed. N. Piskunov, W. W. Weiss, & D. F. Gray, Vol. 210, A20  
 Danby, J. M. A. & Burkardt, T. M. 1983, Celestial Mechanics, 31, 95  
 de Medeiros, J. R. & Udry, S. 1999, A&A, 346, 532  
 Desort, M., Lagrange, A. M., Galland, F., Udry, S., & Mayor, M. 2007, in SF2A-2007: Proceedings of the Annual meeting of the French Society of Astronomy and Astrophysics, ed. J. Bouvier, A. Chalabaev, & C. Charbonnel, 402  
 Donati, J.-F., Semel, M., Carter, B. D., Rees, D. E., & Collier Cameron, A. 1997, MNRAS, 291, 658  
 Ducati, J. R. 2002, VizieR Online Data Catalog: Catalogue of Stellar Photometry in Johnson’s 11-color system., CDS/ADC Collection of Electronic Catalogues, 2237, 0 (2002)  
 Eker, Z. 1989, MNRAS, 238, 675  
 Folsom, C. P., Kochukhov, O., Wade, G. A., Silvester, J., & Bagnulo, S. 2010, MNRAS, 407, 2383  
 Fried, R. E., Eaton, J. A., Hall, D. S., et al. 1982, Ap&SS, 83, 181  
 Gaia Collaboration, Vallenari, A., Brown, A. G. A., et al. 2023, A&A, 674, A1  
 Gray, D. F. 2022, The observation and analysis of stellar photospheres  
 Gustafsson, B., Edvardsson, B., Eriksson, K., et al. 2008, A&A, 486, 951  
 Hall, D. S. 1972, PASP, 84, 323  
 Harris, C. R., Millman, K. J., van der Walt, S. J., et al. 2020, Nature, 585, 357  
 Hatzes, A. P. 2002, Astronomische Nachrichten, 323, 392  
 Hensberge, H., Ilijić, S., & Torres, K. B. V. 2008, A&A, 482, 1031  
 Ilyin, I. 2012, Astronomische Nachrichten, 333, 213

## Appendix A: Extra tables

**Table A.1.** Observing log for STELLA-SES data.

Date (UT)	BJD	Orbital Phase	$V_A$ [km s $^{-1}$ ]	$V_B$ [km s $^{-1}$ ]	$O - C$ [m s $^{-1}$ ]	S/N
2022-03-01	2459640.705	0.581	45.895	-39.906	337.101	257
2022-03-04	2459643.713	0.686	35.085	-28.993	-92.433	247
2022-03-06	2459645.697	0.756	20.870	-12.878	-44.386	311
...						
...						
2022-11-09	2459893.322	0.419	-28.937	35.485	-0.0381	327
2022-11-10	2459894.320	0.454	-37.279	42.412	-0.647	354
2022-11-15	2459900.320	0.664	-33.167	38.666	-0.108	347

**Notes.** Complete table is available at the CDS.

**Table A.2.** Observing log for PEPSI-VATT data.

Date (UT)	BJD	Orbital Phase	$V_A$ [km s $^{-1}$ ]	$V_B$ [km s $^{-1}$ ]	$O - C$ [m s $^{-1}$ ]	S/N
2022-05-10	2459709.827	0.002	-30.964	45.862	215.251	408
2022-05-10	2459709.891	0.035	-31.217	45.608	201.551	415
2022-05-11	2459710.843	0.037	-34.147	48.685	-17.853	406
...						
...						
2022-06-07	2459737.903	0.982	-28.824	43.197	225.099	405
2022-06-13	2459743.967	0.194	-23.766	36.844	-399.837	422
2022-06-14	2459744.836	0.224	-17.650	30.947	-259.443	716

**Notes.** Complete table is available at the CDS.

**Table A.3.** Period analysis of HR 7275 for different activity indicators.

Activity Indicator	$P_{LS}$ (days)	$P_{PDM}$ (days)
Ca II IRT-2	$28.0 \pm 0.1$	$28.0 \pm 0.2$
Ca II H	$27.8 \pm 0.1$	$27.8 \pm 0.3$
Ca II K	$27.8 \pm 0.1$	$27.8 \pm 0.3$
H $\alpha$	$14.2 \pm 0.4$	$14.2 \pm 0.5$
$\Delta T$	$28.2 \pm 0.1$	$14.2 \pm 0.1$
RV residuals	$13.6 \pm 0.3$	$27.2 \pm 0.4$

**Notes.** Rotational period is determined by using different activity indicators with two methods; Lomb-Scargle (LS) and phase dispersion minimization (PDM). While the Ca II IRT and H&K lines demonstrate emission modulation with approximately the orbital period ( $\approx 28$  days), the H $\alpha$  and RV residuals show half-period ( $\approx 14$  days) due to the configuration by multiple spots.

## Appendix B: Extra figures

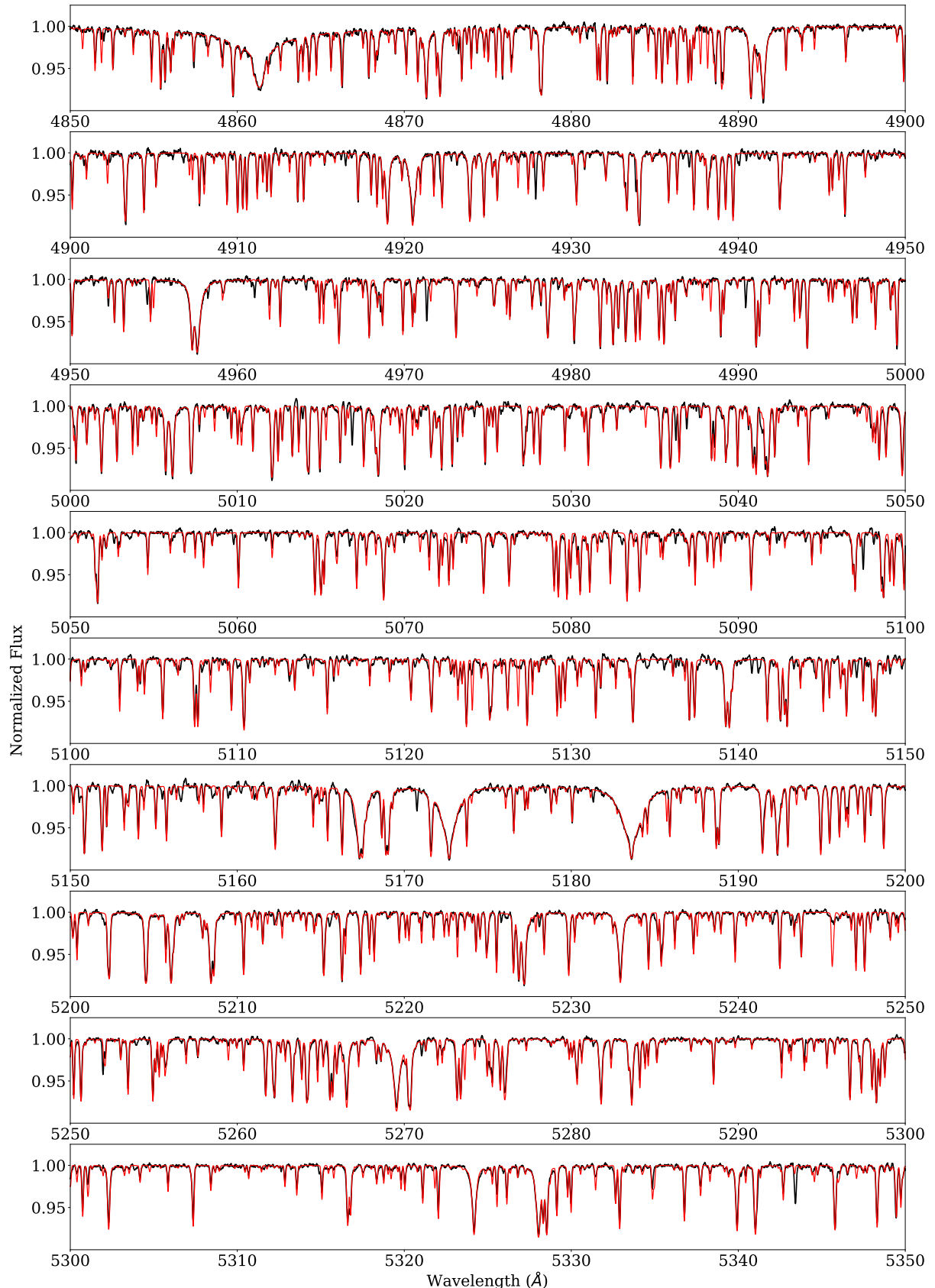


**Fig. B.1.** Mean spectrum of the secondary star in the CD-III range of PEPSI (4800–5400 Å). The black line is the observation, the red line is a model fit based on ParSES and MARCS.

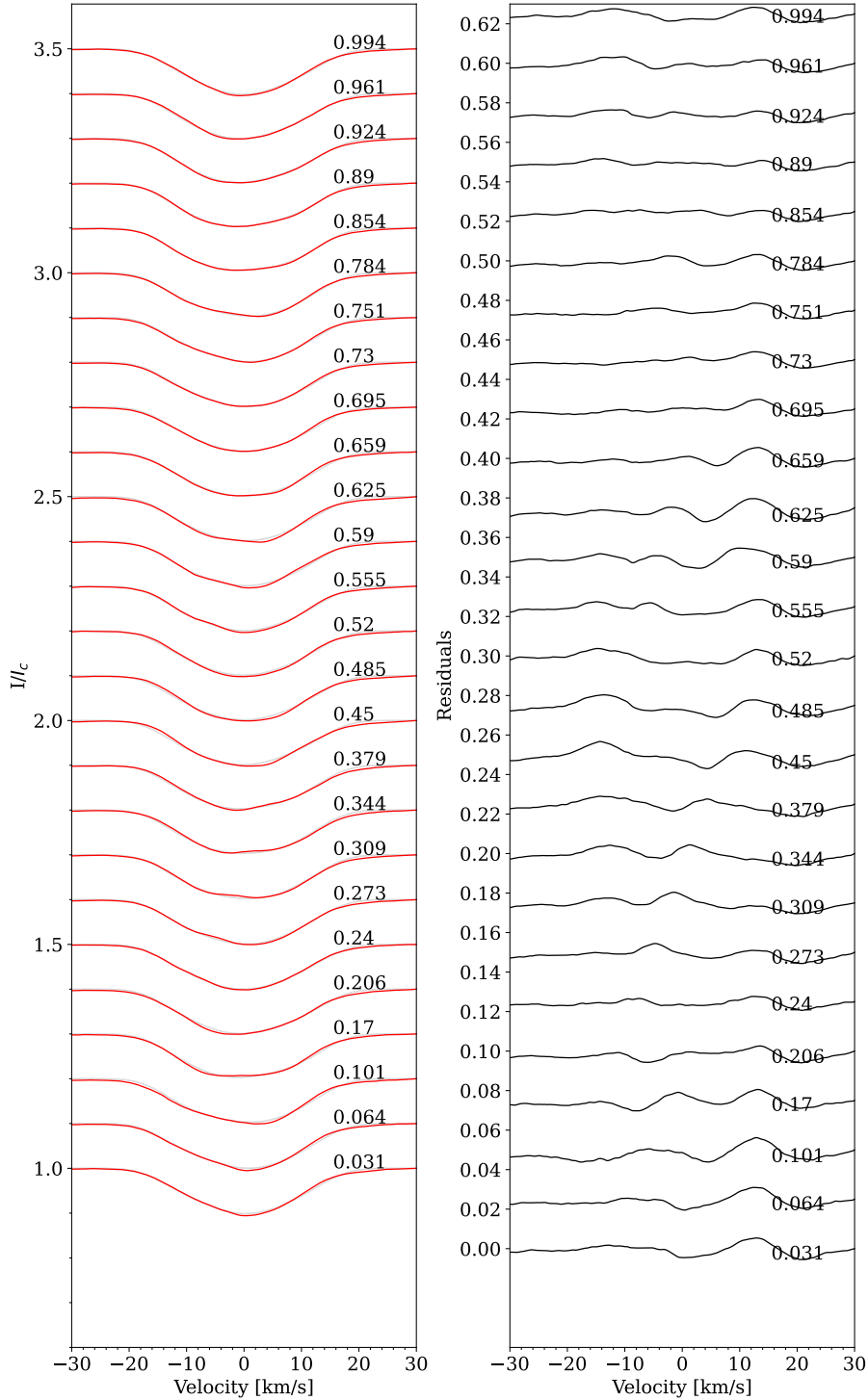


**Fig. B.2.** LSD profiles for the *iMAP* inversions. On the left panel the observed line profiles (red line) are compared with the fitted synthetic profiles (black dotted lines). The corresponding residuals are plotted in the right panel. Numbers on the right side of each panel indicate the rotational phase.

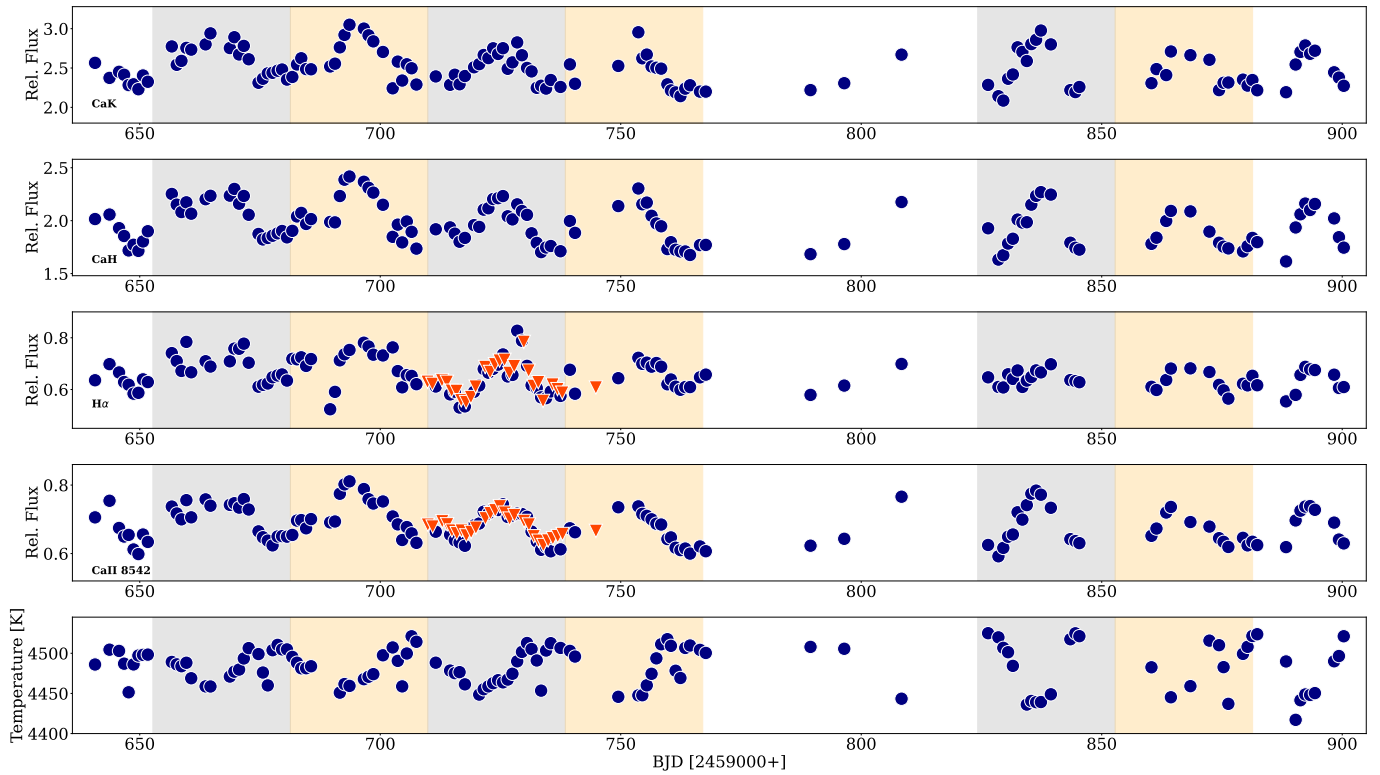


**Fig. B.3.** Chromospheric line emissions and effective temperature versus time. The dark blue circles indicate the STELLA observations while red triangles show the PEPSI data set. Consecutive complete rotations are shaded with gray and orange colors.